

Efficient generation of divergent and collimated hot electrons via a novel multi-beam two-plasmon decay and stimulated Raman scattering mechanism

K.Y. Meng,¹ Z.H. Cai,¹ J. Li,^{1, 2, a)} C. Yao,^{1, 3} L. Hao,³ F.X. Zhou,⁴ R. Yan,^{4, 2, b)} and J. Zheng^{1, 2}

¹⁾*Department of Plasma Physics and Fusion Engineering and CAS Key Laboratory of Geospace Environment, University of Science and Technology of China, Hefei, Anhui 230026, People's Republic of China.*

²⁾*Collaborative Innovation Center of IFSA (CICIFSA), Shanghai Jiao Tong University, Shanghai 200240, People's Republic of China*

³⁾*Institute of Applied Physics and Computational Mathematics, Beijing 100088, People's Republic of China*

⁴⁾*Department of Modern Mechanics, University of Science and Technology of China, Hefei, Anhui 230026, People's Republic of China.*

(Dated: 22 October 2024)

In inertial confinement fusion (ICF) implosions, the preheating risks associated with hot electrons generated by laser plasma instabilities (LPI) are contingent upon the angular characteristics of these hot electrons for a given total energy. Using particle-in-cell simulations, we reveal a novel multi-beam collaborative mechanism of two-plasmon decay (TPD) and stimulated Raman scattering (SRS), and investigate the angular variations of hot electrons generated from this shared TPD-SRS (STS) instability driven collectively by dual laser beams with varying incident angles θ_{in} (24° to 55° at the incident plane) for typical ICF conditions. In the simulations with $\theta_{in} \gtrsim 44^\circ$, STS emerges as the dominant mechanism responsible for hot electron generation, leading to a wide angular distribution of hot electrons that exhibit both pronounced divergent and collimated components. The common Langmuir wave associated with STS plays a crucial role in accelerating both components. By properly modeling the STS common wave gains, we establish scaling relations between these gains and the energies of collimated and divergent hot electrons. These relations reveal that the divergent hot electrons are more sensitive to variations in gain compared to the collimated electrons. Additionally, the calculated gains qualitatively predict the asymmetry in hot electron angular distributions when the density gradients deviate from the bisector of the laser beams. Our findings offers insights for hot electron generation with multiple beams, potentially complementing previous experiments that underscore the critical role of overlapped intensity from symmetric beams within the same cone and the dominance of dual-beam coupling.

I. INTRODUCTION

In inertial confinement fusion (ICF), a spherical capsule is imploded by multiple high-power laser beams to compress the central fuels to extreme density and pressure, thereby initiating self-sustained fusion reactions¹. During the implosion, hot electrons (with energy above ~ 50 keV) produced by laser plasma instabilities (LPI)² can preheat the uncompressed fuel and degrade the implosion^{3,4}. In most ICF schemes^{5–8}, such hot electrons need to be reduced to improve the implosion, except for shock ignition⁹ (SI), in which hot electrons generated during the spike pulse can enhance the shock pressure^{10,11} and enhance the compression. While ignition has been achieved using the indirect-drive scheme on the NIF laser facility¹² with hot electron threats minimized by unique experimental configurations, the pursuit of higher energy gains^{13,14} and alternative ignition schemes^{6–9,15,16} still demands effective control and thorough characterization of hot electron effects. Thus, reliably characterizing the properties of hot electrons is crucial to evaluating their potential detrimental or beneficial impacts.

Previous ICF experiments have explored the hot electron energy and temperature scaling relations under various laser-

plasma conditions^{17,18}. One primary source of these hot electrons has been identified as two-plasmon decay (TPD), a major LPI in both direct^{19,20} and indirect²¹ ICF schemes. In TPD, one laser wave decays into two electron plasma waves (EPW), efficiently transferring energy to the EPWs², which can accelerate background electrons. In addition to experimental studies, scaling laws have been examined through first-principle particle-in-cell (PIC) simulations^{22,23}, considering both TPD and stimulated Raman scattering (SRS)—another key LPI that generates hot electrons^{24,25}. In SRS, a laser wave decays into an EPW and an electromagnetic wave (EMW)². In prior direct-drive ICF experiments, TPD has been recognized as the primary source of hot electrons^{17,19,20,26}, except under NIF experimental conditions involving high electron thermal temperature (4–5 keV) and long density scale length ($500\text{--}700\mu\text{m}$), where SRS dominates hot electron generation^{24,27}.

Various approaches have been developed to mitigate hot electron generation, including advancements in target design²⁸ and broadening of laser bandwidths^{29–36}. These studies primarily focus on the suppression of the total hot electron energy. Nevertheless, uncertainties remain concerning the angular distribution of hot electrons. Given hot electron energy and temperature, the impact of hot electrons depends on their angular characteristics. In conventional center hot-spot ignition for both direct³ and indirect drive²⁵ ICF, directional hot electrons that propagate towards the capsule center pose a greater preheating threat than those moving later-

^{a)}Corresponding author: junlisu@ustc.edu.cn

^{b)}Corresponding author: ruiyan@ustc.edu.cn

ally. Similarly, the SI scheme benefits from directional hot electrons to augment the shock pressure. Conversely, in the emerging double-cone ignition (DCI) scheme⁷, hot electrons generated in the compression cone and moving laterally may preheat the ignition cone, forming local pre-plasmas that reduce the energy coupling efficiency of the picosecond ignition laser pulse to the compressed fuel^{37,38}.

Experiments have demonstrated that the angular distribution of hot electrons varies with laser illumination geometry and plasma conditions. Early studies³⁹ involving single-beam CO_2 laser pulses interacting with long-scale-length plasmas have revealed that hot electrons are concentrated at 45° relative to the laser incident direction in the polarization plane. In contrast, more recent experiments⁴⁰ on the OMEGA laser facility have observed a wide divergence of hot electrons during implosions of spherical targets illuminated by 60 laser beams, which agrees well with the PIC simulations^{41,42}. In subsequent SI-relevant experiments⁴³ on the OMEGA-EP laser facility, where intense single-beam laser pulses (with intensities of $5 - 10 \times 10^{15} W/cm^2$) interacted with planar targets, the measured hot electrons associated with both TPD and SRS⁴⁴ exhibited directional characteristics. A more comprehensive experimental study⁴⁵ using single laser beam at varying intensities has shown that the angular distributions of hot electrons varies depending on the specific laser and target configurations. The broad angular spread of hot electrons is generally attributed to the wide EPW spectrum in the nonlinear phase of TPD^{46,47}, while the SRS hot electrons are considered more directional⁴⁷. Nevertheless, the mechanisms behind the generation of hot electrons with various angular features remain insufficiently understood. A key factor influencing these angular characteristics is the laser beam geometry, as the daughter EPWs in TPD and SRS are primarily driven by wave vector matching across multiple laser beams in current ICF experiments^{46,48}.

In this article, we investigate the angular variations of hot electrons in relation to laser illumination geometry using fully kinetic PIC simulations and theoretical analysis. Our results demonstrate that laser geometry is the primary determinant of the angular features of hot electrons, which are mainly driven by a novel shared TPD-SRS (STS) mechanism for moderate or high incident angles. These hot electrons exhibit both pronounced divergent and collimated components, differing from previous understanding, where SRS mainly produces collimated hot electrons and TPD generates widely spread hot electrons. In our study, we specifically focus on dual laser beams symmetric to the density gradient, as the theoretical model we developed under symmetric configurations is also capable of accounting for asymmetry. There are two key reasons for emphasizing the symmetric dual beam cases. First, these configurations can be extended to more beams within the same incident cone, where the overlapped intensity plays a dominant role in hot electron generation^{17,21}. Second, typical OMEGA-EP experiments have shown the dominance of dual-beam coupling rather than more beams in TPD growth⁴⁹. We study incident angle θ_{in} ranging from 24° to 55° , as $\theta_{in} \sim 60^\circ$ brings the laser reflection density near the quarter-critical density $n_c/4$, lowering the TPD threshold—a scenario already

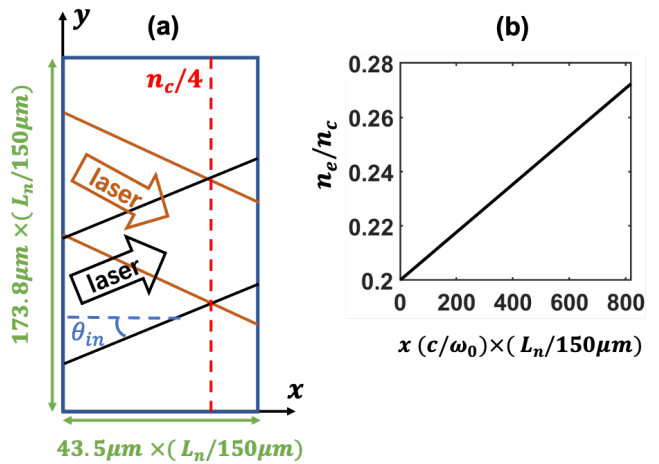


FIG. 1. (a) Schematic setup used in 2D PIC simulations. Note that the figure is not drawn to scale. (b) The density profile along x -direction.

TABLE I. The simulation parameter sets

Index	$I_{ovr} (\times 10^{14} W/cm^2)$	$\theta_{in} (^\circ)$	$L_n (\mu m)$	$T_e (keV)$	$T_i (keV)$	η
i	5.0	24,32,40,	150	3	1.5	1.04
		44,48,52,				
		55				
ii	3.6	24,40,52	150	2	1	1.12
iii	10.0	24,40,52	75	3	1.5	1.04
iv	2.5	24,40,52	300	3	1.5	1.04
v	5.0	52	150	2	1	1.57
vi	6.3	52	150	2	1	1.97

addressed in previous work^{50,51}. Higher θ_{in} values shift the reflection density away from $n_c/4$ to lower density region, making TPD instability unlikely.

This article is organized as follows. Section II describes the simulation setup. In Section III, we provide simulation results with theoretical explanations and discuss the underlying physics. Section IV offers further discussion on the applicability of our results to realistic experimental conditions, Section V presents the conclusions of this study.

II. SIMULATION SETUP

We perform a series of two-dimensional PIC simulations using OSIRIS⁵² code to investigate the interactions of CH plasmas with linear density profiles and dual incident laser beams with incident angles of $\pm\theta_{in}$ relative to the direction of the density gradient, as shown in figure (1). In these simulations, the domain sizes and the laser beam widths are scaled proportionally to the plasma density scale length L_n in order to preserve the same plasma density range and maintain the configuration of the laser beam overlap region. The laser beams are consistently focused on the center of the $n_c/4$ surface, with transverse Gaussian profiles characterized by an

e-folding width of approximately $1130c/\omega_0$ ($\sim 60\mu m$) multiplied by $L_n/150\mu m$ for the wave field, where c and ω_0 represent the speed of light in a vacuum and the laser frequency, respectively, for a wavelength $\lambda = 1/3\mu m$. This beam width sufficiently covers the overlap regions necessary for the growth of TPD. Notably, for the largest $\theta_{in} = 55^\circ$, the beams begin to overlap at $0.215n_c$, which is below the Landau cutoff density for TPD growth.

The overlapped laser intensity I_{ovr} (twice of the single beam intensity I_{sig}), incident angle θ_{in} , initial electron density $n_e(x)$, density scale length $L_n = n_e/(dn_e/dx)$ at $n_e = n_c/4$, as well as electron and ion temperatures T_e, T_i are chosen within specific ranges of $(2.5, 10) \times 10^{14} W/cm^2$, $(24^\circ, 55^\circ)$, $(0.2, 0.272)n_c$, $(75, 300)\mu m$, $(2, 3)keV$ and $(1, 1.5)keV$, respectively, as listed in table (I). We define $I_{sig} = I_{ovr}/2$ as the beam intensity averaged along transverse direction (y-direction) within the e-folding width of the wave field with Gaussian transverse profiles. These conditions are typical for direct-drive ICF experiments with the TPD threshold⁵³ factor $\eta = I_{ovr}L_n\lambda/T_e/81.86$ from 1.04 (right above threshold $\eta = 1$) to 1.97, where I_{ovr} , L_n , λ and T_e should be in unit of $10^{14} W/cm^2$, μm , μm and keV , respectively. We deliberately avoid higher η , or longer L_n and higher T_e to focus on a regime dominated by multi-beam effects rather than single-beam processes. In our simulations, the reflectivity caused by SRS and stimulated Brillouin scattering (SBS) remains below 3% and 7%, respectively, except for the SBS reflectivity of 11% for the simulation (iii) of table I with $\theta_{in} = 52^\circ$.

At time $t = 0$, the p-polarized laser pulses are launched at the left boundary ($x = 0$) of the simulation domain. For the simulations with $L_n = 150\mu m$, the domain size is $L_x \times L_y = 819.2c/\omega_0 \times 3276.8c/\omega_0$ (or $43.5\mu m \times 173.8\mu m$) consisting of 4096×16384 square cells with size $dx = dy = 0.2c/\omega_0$ ($0.011\mu m$). Each cell is initially distributed 200 numerical particles (100 electrons, 50 fully ionized Carbon ions and 50 Hydrogen ions). It is worth noting that the cell size remains the same for all the simulations with varying domain sizes. The simulations progress with a time step of $dt = 0.1414\omega_0^{-1} = 0.025fs$ until $\sim 6ps$ when TPD has mostly reached a quasi-steady state. We employ open field boundaries and thermal particle boundaries along both x- and y-directions. During the simulations, we record all the hot electrons crossing the boundaries with energies exceeding 50 keV. The electromagnetic fields are diagnosed using the time Fourier transform (TFFT) module^{22,54} with time windows of $\sim 1ps$. This module records the time Fourier-transformed fields throughout the entire space but only within specific frequency ranges: $(0.45, 0.55)\omega_0$ for Langmuir waves, $(0.95, 1.05)\omega_0$ for light waves. With frequency filtering, this method provides cleaner signals than the conventional spatial Fourier transform of the ‘‘snapshots’’, which is also employed in our analysis, and can distinguish the directions of different wave modes.

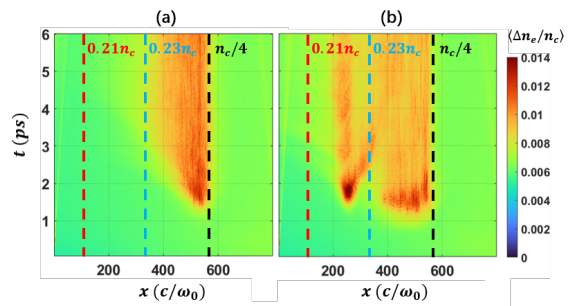


FIG. 2. The space (x -direction) and time evolution of the electron density perturbation $\langle \Delta n_e \rangle$ for the incident angle 24° and 52° in simulation series (i) [Table I]. The x -locations of $0.21n_c$, $0.23n_c$ and $n_c/4$ are marked by vertical dashed lines in red, blue and black colors, respectively.

III. RESULTS AND DISCUSSIONS

A. Two major characteristics of TPD growth for varying θ_{in}

To illustrate the effects of θ_{in} on TPD growth, we first present the results of the simulations with identical physical parameters but varying θ_{in} , as listed in table I(i). These conditions correspond to conventional TPD threshold⁵³ factor $\eta = 1.04$, slightly above the threshold of $\eta = 1$ to represent a typical TPD-dominant case. As θ_{in} increases from 24° to 55° , the TPD growth primarily exhibits two distinct characteristics for relatively smaller ($\theta_{in} < 40^\circ$) and larger ($\theta_{in} > 44^\circ$) incident angles, respectively. The two characteristics can be effectively demonstrated by typical cases of $\theta_{in} = 24^\circ$ and 52° . For these cases, the space (x -direction) and time evolution of electron density perturbations, mainly produced mainly by the TPD daughter EPWs, are plotted in figure 2(a) and 2(b), respectively. The color scale in the two figures represents $\langle \Delta n_e \rangle (x, t)$, which is the perturbation level at certain location x and time t :

$$\langle \Delta n_e \rangle (x, t) = \sqrt{\frac{\sum_{i_y=1}^{N_y} [n_e(x, dy \cdot i_y, t) - n_e(x, dy \cdot i_y, 0)]^2}{N_y}} \quad (1)$$

where i_y is the cell index along y -direction, and N_y is total the cell number along y -direction of the simulation domain.

The growth of TPD modes at different times can be demonstrated by $\langle \Delta n_e \rangle (x, t)$ in figure (2). For $\theta_{in} = 24^\circ$, TPD modes first grow near $n_c/4$, then diffuse to $\sim 0.23n_c$ and reach the quasi-steady state after $\sim 3ps$. By contrast, TPD modes for $\theta_{in} = 52^\circ$ initially grow in a much broader space range from $0.22n_c$ to $n_c/4$, and this range remains until TPD reaches a quasi-steady state.

The different behaviors of $\langle \Delta n_e \rangle (x, t)$ correspond to distinct EPWs of TPD daughter waves with frequency $\sim \omega_0/2$. The space spectra of the electric fields with frequency from $0.45\omega_0$ to $0.55\omega_0$ are plotted in figure 3 for two time intervals: 1 to 2ps and 5 to 6ps, representing the linear and non-

linear stages, respectively. To equally reflect the electric fields along x - and y - directions, we define $|E|$ as the magnitude of electric fields in k_x and k_y phase space with frequency from $0.45\omega_0$ to $0.55\omega_0$:

$$|E| = |E(k_x, k_y)| = \sqrt{E_x(k_x, k_y)^2 + E_y(k_x, k_y)^2} \quad (2)$$

where E_x and E_y are the electric fields along x - and y - directions. For $\theta_{in} = 24^\circ$, TPD grows significantly near the crossing point of the two TPD hyperbolas of the two incident beams in the linear stage [figure (3a)], agreeing with the typical growth mechanism of sharing a forward-going common wave⁵⁵. In the later nonlinear stage, when the quasi-steady state is formed, the spectrum broadens due to nonlinear saturations⁵⁶, though the common wave signals remain dominant.

The excitation of such common wave relies on the crossing of the hyperbolas in the forward direction (positive x -direction) [figure (3a)(3c)], which is not satisfied for $\theta_{in} = 52^\circ$ [figure (3b)(3d)]. In this case, the hyperbolas intersect at the sides with EPWs observed near the intersections. One might intuitively guess they are common waves co-driven by two laser beams via TPD. However, this cannot be the case, as the common wave cannot simultaneously act as the daughter wave with relatively longer \vec{k} (common wave frequency $\omega_{co} > \omega_0/2$) for one laser beam and shorter \vec{k} ($\omega_{co} < \omega_0/2$) for the other beam when both beams have the same frequency ω_0 .

We also observe electric field modes at $k_x \sim 0$ with discrete peaks at different k_y 's. The modes with $k_x \sim 0$ and $k_y \sim 1.6k_0$ near the hyperbola have much greater $|k|$ than all the modes for $\theta_{in} = 24^\circ$. According to the TPD theory, these modes should locate at much lower density than the modes for $\theta_{in} = 24^\circ$, agreeing with the results in figure (2). Moreover, the overall electric field spectra for $\theta_{in} = 52^\circ$ are dominated by separated peaks rather than broad signal islands for $\theta_{in} = 24^\circ$, even in the nonlinear stage. This causes multi-peak angular distributions of hot electrons, which are presented in section III C.

B. The excitation mechanism of side TPD modes for relatively larger θ_{in}

For the two characteristics described in the previous section, the one corresponds to $\theta_{in} = 24^\circ$ is driven through a forward-going common wave and has been well understood⁵⁵. Thus, we focus on the underlying physics of the side modes excitation for $\theta_{in} = 52^\circ$. We find that the side EPWs are still common waves, but they are shared by TPD driven by one beam and SRS by the other, instead of two TPDs, so we name it shared TPD-SRS (STS) instability in this article. This STS mechanism can explain most major modes in figure (3b)(3d), especially those side modes with $k_x \sim 0$.

To better illustrate the STS mechanism, we first recall the basic TPD and SRS theories of wave coupling and maximum growth conditions. As typical three-wave coupling processes,

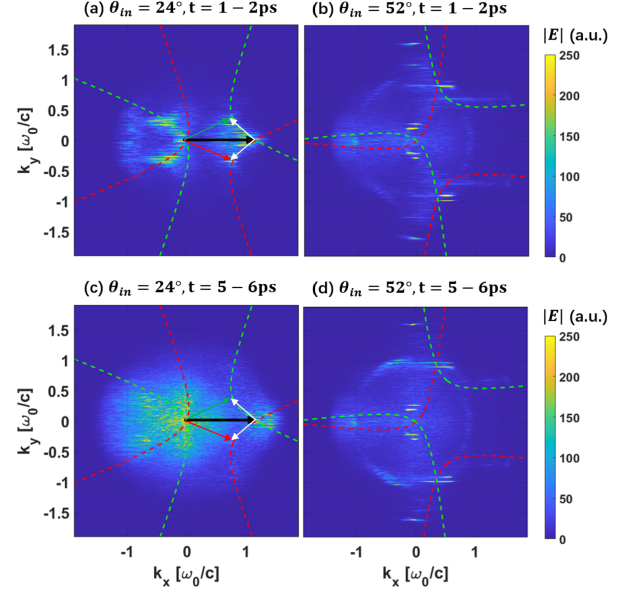


FIG. 3. The space spectra of $|E(k_x, k_y)|$ defined by equation (2) for the simulation (i) [table I] during the time of 1-2ps (a)(b) and 5-6ps(c)(d), and with $\theta_{in} = 24^\circ$ (a)(c) and 52° (b)(d). The TPD hyperbola rotated by $\pm\theta_{in}$ are plotted as dashed curves, representing the locations corresponding to maximum TPD growth rates for the two incident laser beams. In (a)(c), the colored arrows mark the wave vectors of the laser beams (green and red), common EPW (black) and the other TPD modes (white). The corresponding wave vectors for (b)(d) are given in figure 4(b).

both TPD and SRS require matching conditions of frequency $\omega_{0,1,2}$ and wave vector $\vec{k}_{0,1,2}$ to be satisfied for the instability to grow:

$$\vec{k}_0 = \vec{k}_1 + \vec{k}_2 \quad (3)$$

$$\omega_0 = \omega_1 + \omega_2 \quad (4)$$

where the subscripts 0, 1 and 2 refer to the laser wave and two daughter waves, respectively. The $\omega_{0,1,2}$ and $\vec{k}_{0,1,2}$ must follow the dispersion relations of electromagnetic waves (EMWs) [equation (5)] or EPWs [equation (6)], depending on the wave forms:

$$\omega^2 = \omega_{pe}^2 + k^2 c^2 \quad (5)$$

$$\omega^2 = \omega_{pe}^2 + 3k^2 v_{te}^2, \quad (6)$$

where ω_{pe} is the plasma frequency depending on the density n_e , $v_{te} = \sqrt{T_e/m_e}$ denotes the electron thermal speed, where m_e is the electron mass.

Given ω_{pe} and v_{te} (or n_e and T_e), the equations of dispersion relations and matching conditions determine two matching ellipses of TPD and SRS [figure (4a)]. The vectors starting from the origin ending on the ellipses represent all the possible EPW daughter waves satisfying the matching equation (3) to (6). The vectors from the end of k_0 (the horizontal green arrow) to the blue ellipse mark the corresponding wave vectors of scattered lights via SRS.

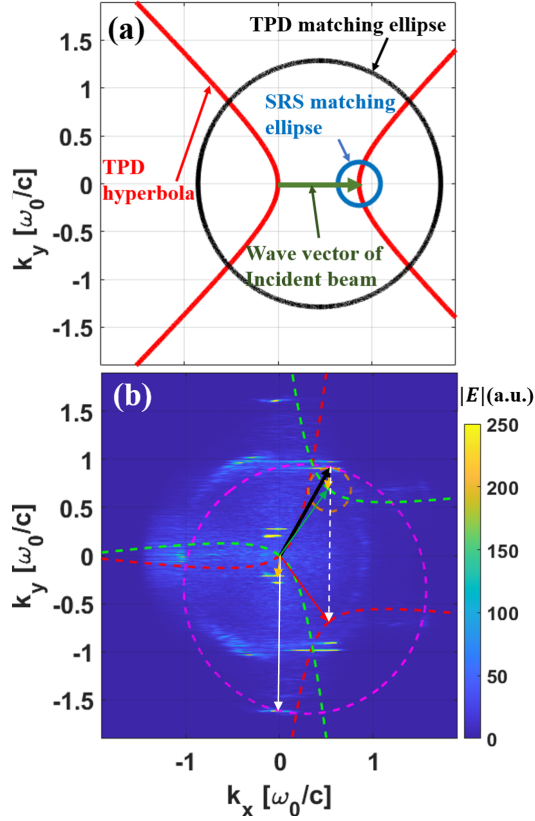


FIG. 4. (a) Schematic view of the matching ellipses of TPD (black) and SRS (blue) in k_x and k_y phase space for a laser beam with wave number (green) $k_0 \sim 0.87\omega_0/c$ for a certain n_e . The red hyperbola $k_y^2 = k_x(k_x - k_0)$ corresponds to the wave numbers with the greatest TPD growth rates for different n_e . For relatively higher n_e , the ellipses are smaller. (b) The space spectra of $|E(k_x, k_y)|$ defined by equation (2) for the simulation (i) [table I] with $\theta_{in} = 52^\circ$ during the simulation time of 5-6ps.

With the above theory of matching ellipses, we can conveniently identify all the common waves that can be co-driven by multiple incident laser beams. In figure (4b), We redraw the $|E|$ spectrum for $\theta_{in} = 52^\circ$ case during 5-6 ps [figure (3d)] with the TPD ellipse (purple dashed line) for the laser beam pointing down-right and the SRS ellipse (brown dashed line) for the laser beam pointing up-right for $n_e = 0.217n_c$ and $T_e = 3keV$ [table I(i)]. The two ellipses intersect in k space, suggesting the EPW pointing from the origin to the intersection can be co-driven by the two laser beams via TPD and SRS.

Nonetheless, the formation of such common waves does not guarantee strong growth, which requires high gain of the driven modes. Actually, the matching of the common waves broadly exists for a considerable density range between $0.21n_c$ and $0.23n_c$, wherever the two matching ellipses intersect. However, only one dominant common wave among these matching modes can grow significantly, as shown in the simulation results [figure (4b)].

To determine the relative significance of all the matching modes, we adopt the Rosenbluth gain⁵⁷ G_R , which physi-

cally means the amplification factor of a delta-function seed in nonuniform plasmas:

$$G_R = \exp\left[\frac{\pi\gamma_0^2}{\kappa'V_1V_2}\right] \quad (7)$$

where γ_0 is the temporal growth rate of the instability in a homogeneous plasma, V_1 and V_2 are the group velocities of the two daughter waves, and $\kappa' = \frac{d}{dx}(k_{0x} - k_{1x} - k_{2x})$ denotes the k mismatch factor along the x -direction (along the density gradient). The above equation (7) applies to both TPD and SRS with all the variables varying for different n_e and T_e . For simplicity, we do not write this equation separately for TPD and SRS, and all the following equations apply for both TPD and SRS unless otherwise stated.

Using Rosenbluth gain theory, the total gain of the STS common waves driven simultaneously by TPD and SRS can be evaluated by considering the contributions from both TPD and SRS:

$$G_{tot} = G_S \times G_T \quad (8)$$

where G_S and G_T are the gains of SRS and TPD, respectively. In 1-dimension cases, they are basically Rosenbluth gains described in equation (7). Please note that achieving G_R relies on the complete amplifications process of initial seeds traveling along the density gradient for a finite distance. However, in our simulations using Gaussian beams with finite beam widths, the amplification processes of TPD and SRS seeds which have finite transverse velocities are limited by the transverse size of the laser overlap region [figure (1a)]. Namely, the unstable seeds may leave the laser overlap region and stop growing before reaching G_R . Therefore, the gain should be truncated to the amplification within the laser overlap region, and the gains G_S and G_T should be similarly written as

$$G_S \text{ or } G_T = \min(G_R, G_w) \quad (9)$$

where

$$G_w = \exp\left[\frac{\gamma_0 L_{tr}}{\max(|V_{1y}|, |V_{2y}|)}\right] \quad (10)$$

is the gain assuming the unstable seed continues growing by growth rate γ_0 without saturation during propagation until leaving the laser overlap region from the sides. Here, L_{tr} is the transverse size of the laser overlap region, and V_{1y} and V_{2y} respectively represent the group velocities of the two daughter waves along the transverse (y -) direction. Please note that that the instability growth rate γ_0 for homogeneous plasmas is also the temporal growth rate of the seed propagating in inhomogeneous plasmas⁵⁷. Thus, the minimum value of G_R and G_w should represent the overall gain of the common waves.

With the above analysis, we calculate G_{tot} as a function of n_e with $T_e = 3keV$, $L_n = 150\mu m$ [table I(i)] with $\theta_{in} = 52^\circ$. The results are plotted in figure 5(a). We find that the G_{tot} reaches the highest peak within a narrow density region around $0.217n_c$ with $k_x \approx 0.54$ to $0.57\omega_0/c$ and

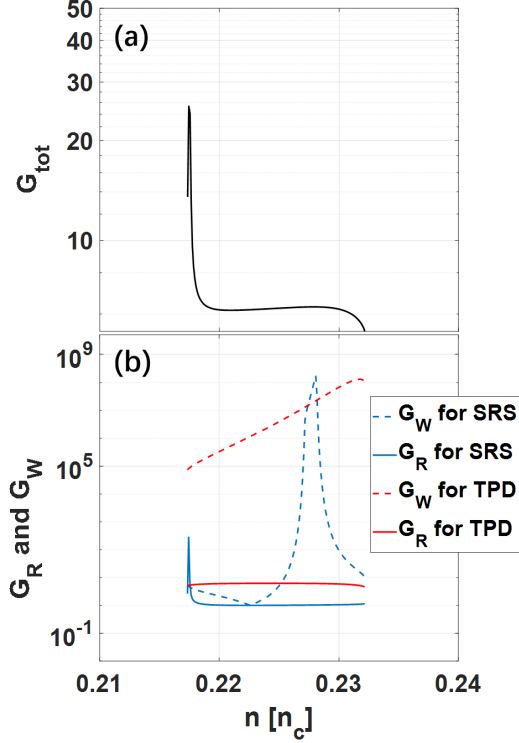


FIG. 5. The calculated (a) G_{tot} , (b) G_R and G_W of TPD and SRS for simulation parameter set (i) in table I with $\theta_{in} = 52^\circ$. The Rosenbluth gain G_R of SRS (blue solid line) is greater than G_W (blue dashed line) near the narrow peak, and does not contribute to G_{tot} .

$k_y \approx 0.91\omega_0/c$. Both the location and the wave number agree very well with the strongest EPW modes observed in figure (4b) and (6a). One may notice another neighboring peak close to the common wave with similar k_x but slightly larger $k_y \approx 0.98\omega_0/c$. This signal is caused by the absolute SRS mode driven by single beams, and is discussed at the end of this section.

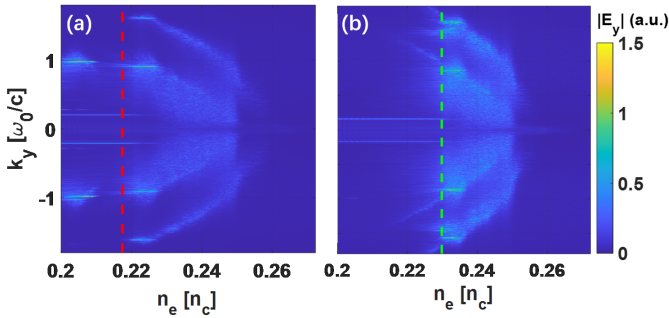


FIG. 6. The $k_y - n_e$ spectra for (a) simulation (i) and (b) simulation (v) [table I] with $\theta_{in} = 52^\circ$ during 5-6 ps. The vertical dashed lines mark the location of the maximum G_{tot} [figure (5a)].

The formation of the common-wave peak relies on the local maximum point of SRS gain G_S , as the TPD gain G_T does not show any local maximum point [figure (5b)]. However,

although the SRS Rosenbluth gain G_R reaches an extremely high peak around the same location due to $\kappa' = \frac{d}{dx}(k_{0x} - k_{1x} - k_{2x}) \approx 0$, it is not the cause of G_S peak, as it is overwritten by the local G_W , as shown by the blue solid and dashed lines in figure (5b).

Additionally, we clarify that the local maximum G_W is not the one with SRS scattered light pointing strictly parallel (0°) to the y-direction. Instead, the strongest SRS scattered light travels along $\theta_s \sim \pm 95^\circ$ to the positive x-direction, according to our calculations. This qualitatively agrees with the simulation results in figure 4(b), where the SRS scattered light covers the band region starting from $(k_x \sim 0, k_y \sim 0.21\omega_0/c)$ and extending to negative k_x , maintaining the same k_y during the propagation. This phenomenon is more clearly depicted in the $k_y - n_e$ spectra of E_y in figure (6), where the horizontal lines with $k_y \sim 0.21\omega_0/c$ represent the propagation of the scattered light towards the negative x-direction. The extension of these lines towards the left boundary of the simulation domain is not expected for the scattered light with $\theta = 90^\circ$, as such light would propagate exclusively along the y-direction, with no component in the x-direction.

In addition to the example discussed above, our theoretical predictions of the peak common wave locations align well with the PIC simulation results under various laser plasma conditions. Figure (6) presents the $k_y - n_e$ phase spaces of E_y overlaid with the peak locations of G_{tot} for the simulation (i) and (v) [table I] with $\theta_{in} = 52^\circ$. In the two $k_y - n_e$ figures, the modes near (a) $0.22n_c$ and (b) $0.23n_c$ with $k_y \sim 0.9\omega_0/c$ are the STS common EPWs, while those at the same density but with much larger k_y correspond to the other paired TPD modes. These figures show that the G_{tot} peak locations consistently match the theoretical STS common wave locations.

In figure (6a), we observe additional modes in the lower density region, exhibiting slightly larger k_y than the common waves. In the $k_x - k_y$ phase space, these modes are situated at $(k_x \sim 0.54\omega_0/c, k_y \sim 0.98\omega_0/c)$ [figure 3(d) and 4(b)], near the band signals of the common waves. We identify these modes as EPWs of absolute SRS modes⁵⁸, with corresponding scattered light at $(k_x \sim 0, k_y \sim 0.28\omega_0/c)$, driven by single laser beams near the incident plane at $n_e \geq 0.2n_c$. This absolute SRS occurs when κ' close to zero. For the simulation (i) with $\theta_{in} = 52^\circ$ at $n_e = 0.2n_c$, our calculations of absolute SRS indicate $(k_x \approx 0.53\omega_0/c, k_y \approx 0.97\omega_0/c)$ for the EPW modes and $(k_x \approx 0.02\omega_0/c, k_y \approx 0.27\omega_0/c)$ for the scattered light, which are in good agreement with the above simulation results. Absolute SRS modes can develop when the laser-plasma conditions surpass the instability threshold⁵⁸. In our simulations, they occur mildly in some cases for which the threshold is slightly exceeded while not observed in others, suggesting they play a negligible role in both hot electron generation and laser reflection.

C. The angular characteristics of hot electrons for different θ_{in}

The driven EPWs can effectively accelerate background thermal electrons with velocity close to the EPW phase veloc-

ity v_{ph} . Therefore, the hot electron characteristics are closely tied to the EPW spectra. For smaller $\theta_{in} = 24^\circ$, the EPW spectra exhibit a two-island structure, as shown in figure (3c). The main island, centered around the origin, contains EPWs with a broad range of wave vectors, which complicates the analysis of the resulting hot electrons. Fortunately, most of these modes have $|k| < 0.5\omega_0/c$, corresponding to $v_{ph} \geq c$, which is significantly greater than the electron thermal velocities, thus inefficient for generating hot electrons. Instead, the smaller island with $k_x > 1\omega_0/c$ and $k_y \sim 0$, leading to $v_{ph} \sim 0.5c$, can efficiently capture and accelerate background electrons with temperatures around a few keV . Correspondingly, as shown in figure (7), the hot electrons accelerated in the case of $\theta_{in} = 24^\circ$ exhibit a collimated feature in the angular distribution. Also, the same feature is observed for $\theta_{in} = 32^\circ$ when the side TPD and SRS common waves are not significantly driven.

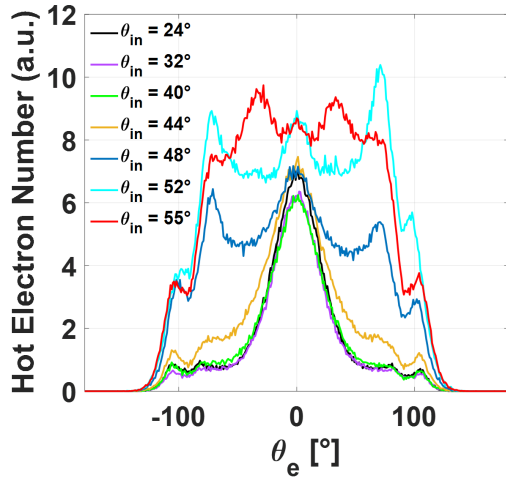


FIG. 7. The angular distribution of hot electrons for the simulation (i) in table I with different laser incident angle θ_{in} 's.

For larger $\theta_{in} = 52^\circ$, the EPW spectra display a multi-peak structure (figure 3d and 4b). Thus, the hot electron characteristics should be determined by these peaks. According to our analysis in the previous section, these peaks mainly correspond to the modes of TPD and SRS co-driven by dual beams, and primarily point sideways. Specifically, the common EPW propagates at $\sim 60^\circ$ to the x-direction, while the other TPD daughter wave has $k_x \sim 0$ and $k_y \sim 1.6\omega_0/c$, perpendicular to the x-direction. These two EPWs should generate hot electrons with high divergent angles. This feature is reflected in the hot electron angular distributions for $\theta_{in} \geq 48^\circ$ [figure (7)] which exhibit pronounced side peaks at $\sim 72^\circ$.

Furthermore, the hot electron angular distributions also show a peak at 0° along the x-direction, corresponding to collimated hot electrons. However, the EPW spectrum does not indicate any EPW modes traveling along the x-direction [figure (4b)]. To address this discrepancy, we find that the collimated hot electrons can be generated by two common EPW modes traveling oblique to x-direction at symmetric angles. Owing to symmetric laser beams, the common EPWs pointing up-right and down-right share the same k_{cx} (the wave number along x-direction) with positive and negative k_{cy} (the wave

number along y-direction). The common EPWs along the two directions can form a forward-going phase of electric field, which can capture and accelerate background electrons similar to an EPW traveling along the x-direction. This can be demonstrated by a brief derivation. We assume $E_{cx1}(x,t)$ and $E_{cx2}(x,t)$ represent the electric fields along the x-direction of the two common EPWs, given by:

$$E_{cx1}(x,t) = E_{cx0} \sin(k_{cx}x + k_{cy}y - \omega_c t + \phi_{c1}) \quad (11)$$

$$E_{cx2}(x,t) = E_{cx0} \sin(k_{cx}x - k_{cy}y - \omega_c t + \phi_{c2}) \quad (12)$$

where E_{cx0} and ω_c are the field amplitude and frequency of the common waves, respectively, with random phases ϕ_{c1} and ϕ_{c2} . The total electric field E_{cx} caused by the common EPWs becomes

$$\begin{aligned} E_{cx} &= E_{cx1}(x,t) + E_{cx2}(x,t) \\ &= 2E_{cx0} \sin(k_{cx}x - \omega_c t + \phi_{c1}/2 + \phi_{c2}/2) \\ &\quad \times \cos(k_{cy}y + \phi_{c1}/2 - \phi_{c2}/2) \end{aligned} \quad (13)$$

which consists of a forward-propagating electric field $\sin(k_{cx}x - \omega_c t)$ with phase velocity $v_{cph} = \omega_c/k_{cx}$, modulated along the y-direction by $\cos(k_{cy}y)$. For this field E_{cx} , the background electrons can be captured and accelerated as if they are being driven by an EPW with $v_{ph} = v_{cph}$ along the x-direction.

The electric field structure described by the equation (13) is observed in the overlap region of the common waves propagating up-right and down-right. This region is situated around $n_e \sim 0.217n_c$ or $x = 193c/\omega_0$ and $y = 1640c/\omega_0 \sim L_y/2$. In this area, although the fields of common waves are always mixed with the fields from the incident laser beams, their spatial spectra are clearly separated. Therefore, we can isolate the spatial distribution of only the common wave fields by applying spectral filtering in the Fourier-transformed space and then performing an inverse Fourier transform. Figure (8a) presents the filtered common wave fields at $t = 1.9ps$, where both longitudinal and transverse modulations are visible around $(k_x = 0.54\omega_0/c, k_y = 0.91\omega_0/c)$, in agreement with the waveform predicted by equation (13). This common wave field should propagate along x-direction and is capable of capturing and accelerating background electrons to collimated hot electrons.

The captured electrons being accelerated by this field can be visualized through the energy density profile of the electrons, defined as:

$$\varepsilon_e(i,j) = \sum_{k=1}^{N_{ij}} w_e (\gamma - 1) \quad (14)$$

where ε_e represents the electron energy density in the cell indexed by (i,j) . The number of electrons in the cell is denoted by N_{ij} , with w_e and γ referring to the charge weight and the relativistic gamma factor of the k -th electron, respectively. In the absence of the accelerated background electrons, ε_e is proportional to $n_e T_e$, which is approximately 1.9×10^{-3} at

$n_e \sim 0.217n_c$. When common waves begin accelerating electrons, the local ε_e will increase in regions where these electrons are located. Figure (8b) depicts the spatial distribution of ε_e , where the yellow bands with $\varepsilon_e > 1.9 \times 10^{-3}$ corresponds to the areas where accelerated electrons are located.

By comparing the common wave field structure [figure (8a)] to the locations of the accelerated electrons [figure (8b)], using the dashed grids as a reference, it becomes evident that the hot electrons are concentrated in bands positioned between the peaks of the common wave fields. The parallel yellow bands along the y-direction suggest that these electrons are being accelerated by the wave fields and are moving along the x-direction. These findings indicate that the symmetric, divergent common waves can produce collimated hot electrons.

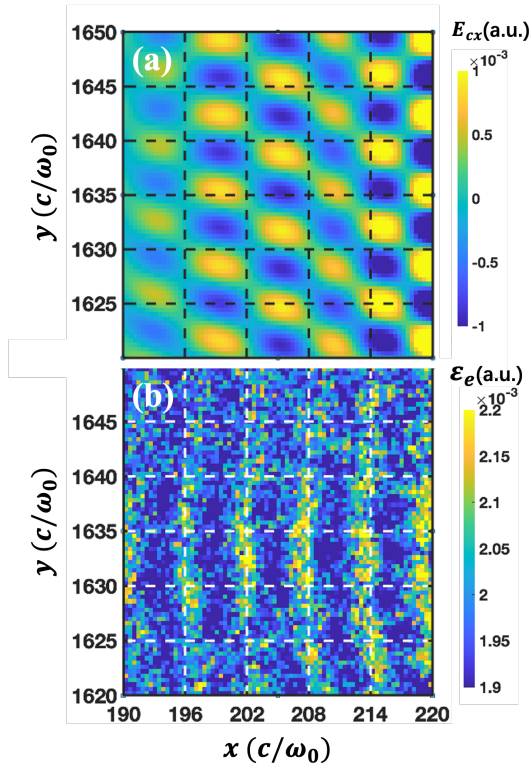


FIG. 8. (a) The E_{cx} fields [equation (13)] of two common waves and (b) electron energy density ε_e [equation (14)] in the overlap region near $n_e = 0.217n_c$ at $t = 1.9ps$ for the PIC simulation (i) [Table I] with $\theta_{in} = 52^\circ$. The dashed grids in the figures illustrate the alignment between the (a) E_{cx} structures and (b) the accelerated electrons. The data in (a) are obtained by filtering the space spectra of the common waves out of the total electric field using Fourier and inverse-Fourier transforms.

D. The energy scaling of hot electrons with different divergent angles

As we discussed in the previous section, hot electrons with different divergent angles are generated through varied mechanisms. Thus, they may follow different energy scalings. According to the divergent angle θ_e , we classify the hot elec-

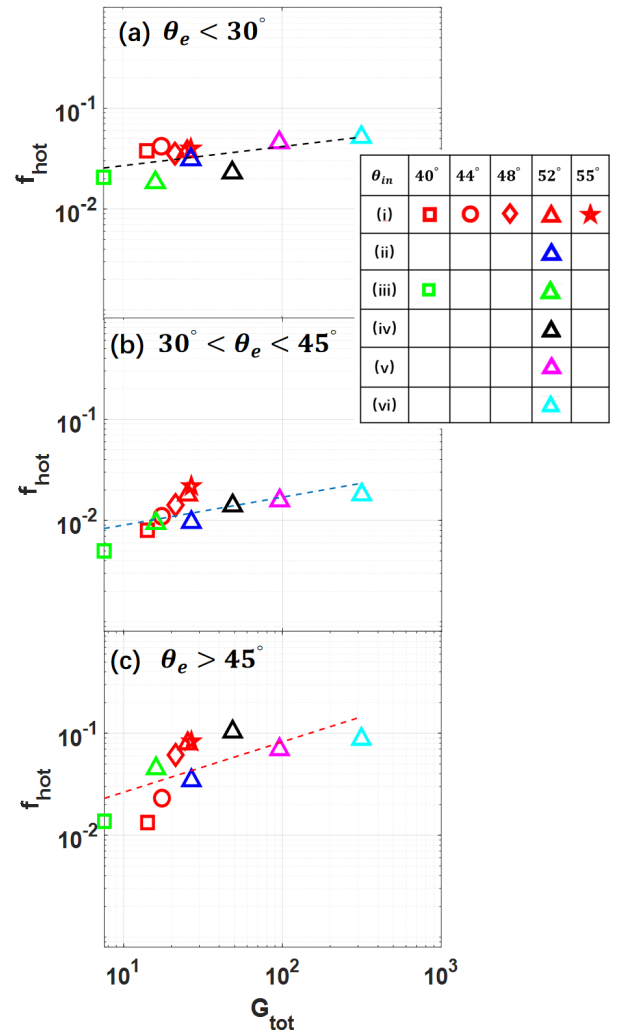


FIG. 9. Scaling relations between energy of hot electrons (f_{hot} normalized by incident beams) with (a) $\theta_e < 30^\circ$, (b) $30^\circ < \theta_e < 45^\circ$ and (c) $\theta_e > 45^\circ$ and G_{tot} of common wave driven by TPD and SRS.

trons into three categories: collimated ($\theta_e < 30^\circ$), intermediate ($30^\circ < \theta_e < 45^\circ$) and divergent ($\theta_e > 45^\circ$). Figure (9) plots the energy fractions of these groups against G_{tot} for the simulations listed in table I, specifically for $\theta_{in} \geq 40^\circ$. Smaller θ_{in} values correspond to the dominant forward dual-TPD common wave mechanism [section III B], rather than the side TPD-SRS common waves, which G_{tot} is based upon. Among these simulations, the results of simulation (ii) and (iv) with $\theta_{in} \geq 40^\circ$ are not given, as the f_{hot} has not reached quasi-steady state till the end of the simulation time due to the weak instability growth.

Our findings show that both the collimated and divergent hot electrons tend to have higher energy than the intermediate group, consistent with the multi-peak angular distributions in figure (7). In this log-log plot, the f_{hot} values of all three groups increase quasi-linearly with G_{tot} , but with notably different slopes. This behavior suggests the following approxi-

mate scaling:

$$f_{hot} \approx CG_{tot}^\alpha \quad (15)$$

where $\alpha = 0.19, 0.28$ and 0.49 , and the coefficient $C = 1.7 \times 10^{-2}, 4.8 \times 10^{-3}$ and 8.5×10^{-3} for the collimated, intermediate and divergent groups of hot electrons, respectively.

The different α values indicate that f_{hot} exhibits varying sensitivity to G_{tot} , which could be related to the differences in acceleration efficiency among the groups. Divergent electrons are accelerated by the common wave and the paired side TPD mode. In the example of the simulation (i) with $\theta_{in} = 52^\circ$, the two modes have $|k| \sim 1.1\omega_0/c$ and $1.6\omega_0/c$, corresponding to phase velocities of $0.45c \sim 5.9v_{te}$ and $0.31c \sim 4.0v_{te}$, respectively. In contrast, according to the equation (13), the collimated hot electrons are accelerated by the moving electric field with phase velocity of $v_{cph} = \omega_c/k_{cx} \sim 0.88c \sim 11.5v_{te}$, much faster than that for divergent hot electrons. These results show that divergent electrons are more easily accelerated due to the lower phase velocity of EPW modes compared to collimated electrons. This difference may account for the varying sensitivity of f_{hot} in response to changes in the amplitude of EPW modes, which is directly related to G_{tot} . A detailed study on the reasons behind these different α values will be the focus of future research.

IV. CONSIDERING REALISTIC EXPERIMENTAL CONDITIONS

A. Effects of asymmetric incidence

In realistic experiments on large-scale laser facilities, despite the symmetric configuration of the beams, the orientation of density contours evolves in space and time during the target surface ablation. As a result, it is common for laser beams to deviate from symmetry relative to the normal of the density contours near $n_c/4$. Therefore, hot electron generation under asymmetric incidence is crucial for accurately assessing f_{hot} in experimental evaluations. In such scenarios, the matching ellipses [Figure (4a)] for both TPD and SRS mechanisms continue to define the common wave modes responsible for the STS mechanism. The cumulative wave amplification at various densities can still be scaled by the total gain, G_{tot} , as derived from equations (7) to (10).

We calculate two new cases using the same physical parameters as case (i) in table (I) but with the laser incident angles directed up-right and down-right ($\theta_{in,up}$, $\theta_{in,down}$) changed from symmetric ($52^\circ, -52^\circ$) to asymmetric configurations of ($48^\circ, -56^\circ$) and ($44^\circ, -60^\circ$). These shifts move the beams away from the density gradient direction by 4° and 8° , as detailed in table (II).

The computed total gains, G_{tot} , for the common waves propagating up-right and down-right, denoted as $G_{tot,up}$ and $G_{tot,down}$, are presented in table (II) for all the three combinations of ($\theta_{in,up}$, $\theta_{in,down}$). From these results, we observe that the asymmetric incident beams lead to variations of up to 28% in $G_{tot,up}$ and $G_{tot,down}$ when compared to the symmetric case. These variations results in differing amplitudes for the two

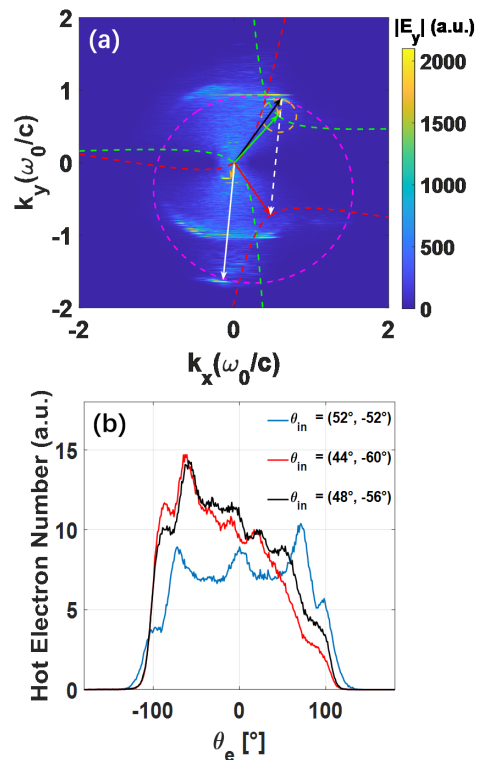


FIG. 10. (a) The space spectra of E_y for the simulation (b) [table II] during the simulation time of 5-6ps. (b) The angular distributions of hot electrons for all the simulations in table II with different θ_{in} 's.

TABLE II. The incident angles and calculated $G_{tot,up}$ and $G_{tot,down}$ for asymmetric incident laser beams.

Index	$\theta_{in,up} (^{\circ})$	$\theta_{in,down} (^{\circ})$	$G_{tot,up}$	$G_{tot,down}$
(a)	52	-52	25	25
(b)	48	-56	28	23
(c)	44	-60	32	20

common wave modes and their associated TPD modes, leading to asymmetric angular distributions of hot electrons. As illustrated in Figure (10a), the amplitude of the common wave propagating up-right (black arrow) is noticeably stronger than that of the wave propagating down-right. For the stronger up-right common wave, the corresponding SRS-scattered light (orange arrow) and the paired TPD mode (white solid arrow), both of which point near the negative k_y direction, exhibit significantly greater strength than those associated with the other down-right common wave.

Due to the asymmetry in $G_{tot,up}$ and $G_{tot,down}$, the angular distributions of hot electrons exhibit an asymmetric shape, as illustrated in figure (10b)]. Interestingly, although $G_{tot,up} > G_{tot,down}$ [table (II)] suggests a stronger common wave propagating in the up-right direction (positive angles), a greater number of hot electrons are produced along negative angles [figure (10b)]. This apparent contradiction arises because the hot electrons are generated by both the common wave and the paired TPD modes. The two waves travel oppositely in y -direction, meaning that hot electrons with positive angles are

influenced by the stronger common wave propagating up-right and the weaker TPD mode paired with the down-right common wave, and *vice versa*. As a result, it is not immediately clear whether more hot electrons will be generated at positive or negative angles. However, the results indicate a greater concentration of hot electrons at negative angles, implying that hot electron generation is more sensitive to the TPD modes with higher $|k|$ and lower phase velocity.

Moreover, the total hot electron energy increases by approximately 20% for asymmetric θ_{in} 's, as the surplus of hot electrons on one side outweighs the reduction on the other.

B. Experimental observability of the STS mechanism

Since the scattered light in the STS mechanism is essentially enhanced SRS scattered light, it should be detectable in experiments. For the simulation (i) [table I] with symmetric incident angle $\theta_{in} = 52^\circ$, if we assume n_e only varies along x -direction in space, the scattered light with a frequency of $\omega \sim 0.512\omega_0$ and wave vector component $k_y \sim 0.212\omega_0/c$ will ultimately have a scattering angle of only $\sim 24^\circ$ relative to the negative x -direction after exiting into the vacuum. This scattered light has the same frequency as the collective Thomson scattering of the incident light on the common EPW mode. Once diagnosed, it should mix with the double-band structure of the TPD $\omega_0/2$ spectra, and strengthen the blue-shift component. This qualitatively agrees with the observations of significantly stronger blue-shift components compared to red-shift components off the target normal direction in previous OMEGA experiments⁵⁹.

C. The actual incident angles in the vacuum

It is important to clarify that all θ_{in} values in this article refer to the incident angles at the density $n_e \sim 0.2n_c$ on the incident plane of our PIC simulations. These angles typically differ from the actual vacuum incident angles, $\theta_{in,vac}$, which are the true parameters defining the beam geometry. We now discuss the relationship between $\theta_{in,vac}$ and θ_{in} by analyzing two extreme cases.

In the first case, where the plasma density is spherically symmetric with the incident beams directed toward the center, we have $\theta_{in,vac} \sim \theta_{in}$. In contrast, for a 1D planar geometry where n_e varies only along the x -axis, the relationship between $\theta_{in,vac}$ and θ_{in} can be determined by the fact that k_y is constant and by using the light wave dispersion relation at $n_e = 0.2n_c$:

$$\theta_{in,vac} \approx \arcsin[0.89\sin\theta_{in}] \quad (16)$$

This yields pairs of $(\theta_{in,vac}, \theta_{in})$ such as $(50^\circ, 60^\circ)$, $(43^\circ, 50^\circ)$, and $(35^\circ, 40^\circ)$. Generally, for a given $\theta_{in,vac}$, the effective incident angle for TPD should lie between $\theta_{in,vac}$ and the calculated θ_{in} from equation (16).

V. CONCLUSION

In this study, we investigate the angular variations of hot electrons generated by multiple laser beams with varying incident angles. We identify a novel multi-beam collaborative process involving two-plasmon decay (TPD) and stimulated Raman scattering (SRS), termed STS, which produces hot electrons with distinct divergent and collimated components.

We demonstrate that the key factor influencing the acceleration of these components is the common Langmuir wave associated with STS. By properly modeling the common wave gain, we obtain scaling relations between the gains and the energy fractions of hot electrons at different angles. Our results show that the energy of divergent hot electrons is more sensitive to variations in the common wave gain. Furthermore, when the density gradient deviates from the bisector of the laser beams—a common occurrence in large-scale laser facilities—our study reveals that asymmetric beam incidence results in unequal common wave gains, leading to asymmetric angular distributions of hot electrons. The stronger peak is observed in the direction opposite to the laser beam with the larger incident angle. These findings highlight potential preheating concerns due to divergent and collimated hot electrons in laser-plasma configurations with high gains in future DCI experiments.

Finally, we observe that the scattered light associated with the STS mechanism qualitatively agrees with previous experimental findings. This scattered light shares the frequency of collective Thomson scattered light from the common wave. Although the onsite scattering angle is large (approximately 95°), the direction of the scattered light shifts towards the density gradient when propagating towards vacuum, with final angle of about 24° in our simulations for 1D plasma density variations. This scattered light merges with the double-band structure of the TPD $\omega_0/2$ spectrum, enhancing the blue-shift component, consistent with prior OMEGA experiments⁵⁹ that observed significantly stronger blue-shift than red-shift signals when viewed off the target normal.

ACKNOWLEDGMENTS

This research was supported by the National Natural Science Foundation of China (NSFC) (Grant Nos. 12275269, 12175229, 12375243, 12275032, 12388101), by the Strategic Priority Research Program of Chinese Academy of Sciences (Grant Nos. XDA25010200 and XDA25050400). The numerical simulations in this paper were conducted on Hefei advanced computing center.

REFERENCES

- ¹S. Atzeni and J. Meyer-ter Vehn, *The Physics of Inertial Fusion: Beam-Plasma Interaction, Hydrodynamics, Hot Dense Matter* (Oxford University Press, Oxford, 2004).
- ²W.L.Kruer, *The Physics of Laser Plasma Interactions* (Westview Press, Boulder CO, 2003).

- ³A. R. Christopherson, R. Betti, C. J. Forrest, J. Howard, W. Theobald, J. A. Delettrez, M. J. Rosenberg, A. A. Solodov, C. Stoeckl, D. Patel, V. Gopalaswamy, D. Cao, J. L. Peebles, D. H. Edgell, W. Seka, R. Epstein, M. S. Wei, M. Gatu Johnson, R. Simpson, S. P. Regan, and E. M. Campbell, “Direct Measurements of DT Fuel Preheat from Hot Electrons in Direct-Drive Inertial Confinement Fusion,” *Physical Review Letters* **127**, 055001 (2021).
- ⁴A. A. Solodov, M. J. Rosenberg, M. Stoeckl, A. R. Christopherson, R. Betti, P. B. Radha, C. Stoeckl, M. Hohenberger, B. Bachmann, R. Epstein, R. K. Follett, W. Seka, J. F. Myatt, P. Michel, S. P. Regan, J. P. Palastro, D. H. Froula, E. M. Campbell, and V. N. Goncharov, “Hot-electron preheat and mitigation in polar-direct-drive experiments at the National Ignition Facility,” *Physical Review E* **106**, 055204 (2022).
- ⁵J. Nuckolls, L. Wood, A. Thiessen, and G. Zimmerman, “Laser compression of matter to super-high densities: Thermonuclear (CTR) applications,” *Nature* **239**, 139–142 (1972).
- ⁶X. T. He, J. W. Li, Z. F. Fan, L. F. Wang, J. Liu, K. Lan, J. F. Wu, and W. H. Ye, “A hybrid-drive nonisobaric-ignition scheme for inertial confinement fusion,” *Physics of Plasmas* **23**, 082706 (2016).
- ⁷J. Zhang, W. M. Wang, X. H. Yang, D. Wu, Y. Y. Ma, J. L. Jiao, Z. Zhang, F. Y. Wu, X. H. Yuan, Y. T. Li, and J. Q. Zhu, “Double-cone ignition scheme for inertial confinement fusion,” *Philosophical Transactions of the Royal Society A: Mathematical, Physical and Engineering Sciences* **378**, 20200015 (2020).
- ⁸K. Lan, “Dream fusion in octahedral spherical hohlraum,” *Matter and Radiation at Extremes* **7**, 055701 (2022).
- ⁹R. Betti, C. D. Zhou, K. S. Anderson, L. J. Perkins, W. Theobald, and A. A. Solodov, “Shock ignition of the thermonuclear fuel with high areal density,” *Physical Review Letters* **98**, 155001 (2007).
- ¹⁰S. D. Baton, A. Colaitis, C. Rousseaux, G. Boutoux, S. Brygoo, L. Jacquet, M. Koenig, D. Batani, A. Casner, E. L. Bel, D. Raffestin, A. Tentori, V. Tikhonchuk, J. Trela, C. Reverdin, L. Le-Deroff, W. Theobald, G. Cristoforetti, L. A. Gizzi, P. Koester, L. Labate, and K. Shigemori, “Preliminary results from the LMJ-PETAL experiment on hot electrons characterization in the context of shock ignition,” *High Energy Density Physics* **36**, 100796 (2020).
- ¹¹A. Tentori, A. Colaitis, W. Theobald, A. Casner, D. Raffestin, A. Ruocco, J. Trela, E. Le Bel, K. Anderson, M. Wei, B. Henderson, J. Peebles, R. Scott, S. Baton, S. A. Pikuz, R. Betti, M. Khan, N. Woolsey, S. Zhang, and D. Batani, “Experimental characterization of hot-electron emission and shock dynamics in the context of the shock ignition approach to inertial confinement fusion,” *Physics of Plasmas* **28**, 103302 (2021).
- ¹²H. Abu-shawareb, “Achievement of Target Gain Larger than Unity in an Inertial Fusion Experiment,” *Physical Review Letters* **132**, 65102 (2024).
- ¹³D. Batani, A. Colaitis, F. Consoli, C. N. Danson, L. A. Gizzi, J. Honrubia, T. Köhl, S. Le Pape, J. L. Miquel, J. M. Perlado, R. H. Scott, M. Tatarakis, V. Tikhonchuk, and L. Volpe, “Future for inertial-fusion energy in Europe: A roadmap,” *High Power Laser Science and Engineering* **11**, e83 (2023).
- ¹⁴Z. Sui and K. Lan, “Driver at 10 MJ and 1 shot/30 min for inertial confinement fusion at high gain: Efficient, compact, low-cost, low laser-plasma instabilities, beam color selectable from $2\omega/3\omega/4\omega$, applicable to multiple laser fusion schemes,” *Matter and Radiation at Extremes* **9**, 1–5 (2024).
- ¹⁵V. Gopalaswamy, C. A. Williams, R. Betti, D. Patel, J. P. Knauer, A. Lees, D. Cao, E. M. Campbell, P. Farmakis, R. Ejaz, K. S. Anderson, R. Epstein, J. Carroll-Nellenbeck, I. V. Igumenshchev, J. A. Marozas, P. B. Radha, A. A. Solodov, C. A. Thomas, K. M. Woo, T. J. Collins, S. X. Hu, W. Scullin, D. Turnbull, V. N. Goncharov, K. Churnetski, C. J. Forrest, V. Y. Glebov, P. V. Heuer, H. McClow, R. C. Shah, C. Stoeckl, W. Theobald, D. H. Edgell, S. Ivancic, M. J. Rosenberg, S. P. Regan, D. Bredesen, C. Fella, M. Koch, R. T. Janezic, M. J. Bonino, D. R. Harding, K. A. Bauer, S. Sampat, L. J. Waxer, M. Labuzeta, S. F. Morse, M. Gatu-Johnson, R. D. Petrasso, J. A. Frenje, J. Murray, B. Serrato, D. Guzman, C. Shuldberg, M. Farrell, and C. Deeney, “Demonstration of a hydrodynamically equivalent burning plasma in direct-drive inertial confinement fusion,” *Nature Physics* **20**, 751–757 (2024).
- ¹⁶C. A. Williams, R. Betti, V. Gopalaswamy, J. P. Knauer, C. J. Forrest, A. Lees, R. Ejaz, P. S. Farmakis, D. Cao, P. B. Radha, K. S. Anderson, S. P. Regan, V. Y. Glebov, R. C. Shah, C. Stoeckl, S. Ivancic, K. Churnetski, R. T. Janezic, C. Fella, M. J. Rosenberg, M. J. Bonino, D. R. Harding, W. T. Shmayda, J. Carroll-Nellenbeck, S. X. Hu, R. Epstein, T. J. Collins, C. A. Thomas, I. V. Igumenshchev, V. N. Goncharov, W. Theobald, K. M. Woo, J. A. Marozas, K. A. Bauer, S. Sampat, L. J. Waxer, D. Turnbull, P. V. Heuer, H. McClow, L. Ceurvorst, W. Scullin, D. H. Edgell, M. Koch, D. Bredesen, M. G. Johnson, J. A. Frenje, R. D. Petrasso, C. Shuldberg, M. Farrell, J. Murray, D. Guzman, B. Serrato, S. F. Morse, M. Labuzeta, C. Deeney, and E. M. Campbell, “Demonstration of hot-spot fuel gain exceeding unity in direct-drive inertial confinement fusion implosions,” *Nature Physics* **20**, 758–764 (2024).
- ¹⁷D. T. Michel, A. V. Maximov, R. W. Short, J. A. Delettrez, D. Edgell, S. X. Hu, I. V. Igumenshchev, J. F. Myatt, A. A. Solodov, C. Stoeckl, B. Yaakobi, and D. H. Froula, “Measured hot-electron intensity thresholds quantified by a two-plasmon-decay resonant common-wave gain in various experimental configurations,” *Physics of Plasmas* **20**, 55703 (2013).
- ¹⁸D. H. Froula, B. Yaakobi, S. X. Hu, P.-Y. Chang, R. S. Craxton, D. H. Edgell, R. Follett, D. T. Michel, J. F. Myatt, W. Seka, R. W. Short, A. Solodov, and C. Stoeckl, “Saturation of the two-plasmon decay instability in long-scale-length plasmas relevant to direct-drive inertial confinement fusion,” *Physical Review Letters* **108**, 165003 (2012).
- ¹⁹W. Seka, D. H. Edgell, J. F. Myatt, A. V. Maximov, R. W. Short, V. N. Goncharov, and H. A. Baldis, “Two-plasmon-decay instability in direct-drive inertial confinement fusion experiments,” *Physics of Plasmas* **16**, 052701 (2009).
- ²⁰D. Turnbull, A. V. Maximov, D. Cao, A. R. Christopherson, D. H. Edgell, R. K. Follett, V. Gopalaswamy, J. P. Knauer, J. P. Palastro, A. Shvydkiy, C. Stoeckl, H. Wen, and D. H. Froula, “Impact of spatiotemporal smoothing on the two-plasmon-decay instability,” *Physics of Plasmas* **27**, 102710 (2020).
- ²¹S. P. Regan, N. B. Meezan, L. J. Suter, D. J. Strozzi, W. L. Kruer, D. Meeker, S. H. Glenzer, W. Seka, C. Stoeckl, V. Y. Glebov, T. C. Sangster, D. D. Meyerhofer, R. L. McCrory, E. A. Williams, O. S. Jones, D. A. Callahan, M. D. Rosen, O. L. Landen, C. Sorce, and B. J. MacGowan, “Suprathermal electrons generated by the two-plasmon-decay instability in gas-filled Hohlraums,” *Physics of Plasmas* **17**, 020703 (2010).
- ²²S. H. Cao, D. Patel, A. Lees, C. Stoeckl, M. J. Rosenberg, V. Gopalaswamy, H. Wen, H. Huang, A. Shvydkiy, R. Betti, and C. Ren, “Predicting hot electron generation in inertial confinement fusion with particle-in-cell simulations,” *Physical Review E* **106**, 1–6 (2022).
- ²³S. H. Cao and C. Ren, “Evolution and hot electron generation of laser-plasma instabilities in direct-drive inertial confinement fusion,” *Physics of Plasmas* **30**, 092701 (2023).
- ²⁴M. J. Rosenberg, A. A. Solodov, J. F. Myatt, W. Seka, P. Michel, M. Hohenberger, R. W. Short, R. Epstein, S. P. Regan, E. M. Campbell, T. Chapman, C. Goyon, J. E. Ralph, M. A. Barrios, J. D. Moody, and J. W. Bates, “Origins and Scaling of Hot-Electron Preheat in Ignition-Scale Direct-Drive Inertial Confinement Fusion Experiments,” *Physical Review Letters* **120**, 055001 (2018).
- ²⁵E. L. Dewald, F. Hartemann, P. Michel, J. Milovich, M. Hohenberger, A. Pak, O. L. Landen, L. Divol, H. F. Robey, O. A. Hurricane, T. Döppler, F. Albert, B. Bachmann, N. B. Meezan, A. J. Mackinnon, D. Callahan, and M. J. Edwards, “Generation and Beaming of Early Hot Electrons onto the Capsule in Laser-Driven Ignition Hohlraums,” *Physical Review Letters* **116**, 075003 (2016).
- ²⁶D. Turnbull, A. V. Maximov, D. H. Edgell, W. Seka, R. K. Follett, J. P. Palastro, D. Cao, V. N. Goncharov, C. Stoeckl, and D. H. Froula, “Anomalous Absorption by the Two-Plasmon Decay Instability,” *Physical Review Letters* **124**, 185001 (2020).
- ²⁷H. Wen, R. Yan, A. V. Maximov, and C. Ren, “Linear regime of two-plasmon decay and stimulated Raman scattering instability near the quarter-critical density in plasmas,” *Physics of Plasmas* **22**, 052704 (2015).
- ²⁸R. K. Follett, J. A. Delettrez, D. H. Edgell, V. N. Goncharov, R. J. Henchen, J. Katz, D. T. Michel, J. F. Myatt, J. Shaw, A. A. Solodov, C. Stoeckl, B. Yaakobi, and D. H. Froula, “Two-plasmon decay mitigation in direct-drive inertial-confinement-fusion experiments using multilayer targets,” *Physical Review Letters* **116**, 155002 (2016).
- ²⁹C. Yao, J. Li, L. Hao, R. Yan, C. Wang, A. Lei, Y.-K. Ding, and J. Zheng, “Anomalous hot electron generation from two-plasmon decay instability driven by broadband laser pulses with intensity modulations,” *Nuclear Fusion* **64**, 106013 (2024).
- ³⁰A. Lei, N. Kang, Y. Zhao, H. Liu, H. An, J. Xiong, R. Wang, Z. Xie, Y. Tu, G. Xu, X. Zhou, Z. Fang, W. Wang, L. Xia, W. Feng, X. Zhao, L. Ji, Y. Cui,

- S. Zhou, Z. Liu, C. Zheng, L. Wang, Y. Gao, X. Huang, and S. Fu, "Reduction of Backward Scatterings at the Low-Coherence Kunwu Laser Facility," *Physical Review Letters* **132**, 35102 (2024).
- ³¹P. Wang, H. An, Z. Fang, J. Xiong, Z. Xie, C. Wang, Z. He, G. Jia, R. Wang, S. Zheng, L. Xia, W. Feng, H. Shi, W. Wang, J. Sun, Y. Gao, and S. Fu, "Backward scattering of laser plasma interactions from hundreds-of-joules broadband laser on thick target," *Matter and Radiation at Extremes* **9**, 015602 (2024).
- ³²Q. K. Liu, L. Deng, Q. Wang, X. Zhang, F. Q. Meng, Y. P. Wang, Y. Q. Gao, H. B. Cai, and S. P. Zhu, "Electron kinetic effects in back-stimulated Raman scattering bursts driven by broadband laser pulses," *Matter and Radiation at Extremes* **9**, 047402 (2024).
- ³³H. H. Ma, X. F. Li, S. M. Weng, S. H. Yew, S. Kawata, P. Gibbon, Z. M. Sheng, and J. Zhang, "Mitigating parametric instabilities in plasmas by sunlight-like lasers," *Matter and Radiation at Extremes* **6**, 55902 (2021).
- ³⁴R. K. Follett, J. G. Shaw, J. F. Myatt, H. Wen, D. H. Froula, and J. P. Palastro, "Thresholds of absolute two-plasmon-decay and stimulated Raman scattering instabilities driven by multiple broadband lasers," *Physics of Plasmas* **28**, 032103 (2021).
- ³⁵Y. Gao, Y. Cui, L. Ji, D. Rao, X. Zhao, F. Li, D. Liu, W. Feng, L. Xia, J. Liu, H. Shi, P. Du, J. Liu, X. Li, T. Wang, T. Zhang, C. Shan, Y. Hua, W. Ma, X. Sun, X. Chen, X. Huang, J. Zhu, W. Pei, Z. Sui, and S. Fu, "Development of low-coherence high-power laser drivers for inertial confinement fusion," *Matter and Radiation at Extremes* **5**, 065201 (2020).
- ³⁶Y. Zhao, S. Weng, M. Chen, J. Zheng, H. Zhuo, C. Ren, Z. Sheng, and J. Zhang, "Effective suppression of parametric instabilities with decoupled broadband lasers in plasma," *Physics of Plasmas* **24**, 112102 (2017).
- ³⁷A. G. MacPhee, L. Divol, A. J. Kemp, K. U. Akli, F. N. Beg, C. D. Chen, H. Chen, D. S. Hey, R. J. Fedosejevs, R. R. Freeman, M. Henesian, M. H. Key, S. Le Pape, A. Link, T. Ma, A. J. MacKinnon, V. M. Ovchinnikov, P. K. Patel, T. W. Phillips, R. B. Stephens, M. Tabak, R. Town, Y. Y. Tsui, L. D. Van Woerkom, M. S. Wei, and S. C. Wilks, "Limitation on prepulse level for cone-guided fast-ignition inertial confinement Fusion," *Physical Review Letters* **104**, 055002 (2010).
- ³⁸J. Li, J. R. Davies, T. Ma, W. B. Mori, C. Ren, A. A. Solodov, W. Theobald, and J. Tonge, "Hot-electron generation from laser-pre-plasma interactions in cone-guided fast ignition," *Physics of Plasmas* **20**, 052706 (2013).
- ³⁹N. A. Ebrahim, H. A. Baldis, C. Joshi, and R. Benesch, "Hot electron generation by the two-plasmon decay instability in the laser-plasma interaction at 10.6 μm ," *Physical Review Letters* **45**, 1179–1182 (1980).
- ⁴⁰B. Yaakobi, A. A. Solodov, J. F. Myatt, J. A. Delettrez, C. Stoeckl, and D. H. Froula, "Measurements of the divergence of fast electrons in laser-irradiated spherical targets," *Physics of Plasmas* **20**, 092706 (2013).
- ⁴¹R. Yan, C. Ren, J. Li, A. V. Maximov, W. B. Mori, Z.-M. Sheng, and F. S. Tsung, "Generating energetic electrons through staged acceleration in the two-plasmon-decay instability in inertial confinement fusion," *Physical Review Letters* **108**, 175002 (2012).
- ⁴²R. Yan, A. V. Maximov, C. Ren, and F. S. Tsung, "Growth and Saturation of Convective Modes of the Two-Plasmon Decay Instability in Inertial Confinement Fusion," *Physical Review Letters* **103**, 175002 (2009).
- ⁴³S. Zhang, C. M. Krauland, J. Peebles, J. Li, F. N. Beg, N. Alexander, W. Theobald, R. Betti, D. Haberberger, E. M. Campbell, R. Yan, E. Borwick, C. Ren, and M. S. Wei, "Experimental study of hot electron generation in shock ignition relevant high-intensity regime with large scale hot plasmas," *Physics of Plasmas* **27**, 23111 (2020).
- ⁴⁴J. Li, S. Zhang, C. M. Krauland, H. Wen, F. N. Beg, C. Ren, and M. S. Wei, "Pump depletion and hot electron generation in long density scale length plasma with shock ignition high intensity laser," *Physical Review E* **101**, 033206 (2020).
- ⁴⁵H. Liu, N. Kang, S. Zhou, H. An, Z. Fang, J. Xiong, K. Li, A. Lei, and Z. Lin, "Emission properties of suprathermal electrons produced by laser-plasma interactions," *Laser and Particle Beams* **35**, 663–669 (2017).
- ⁴⁶J. F. Myatt, J. Zhang, R. W. Short, A. V. Maximov, W. Seka, D. H. Froula, D. H. Edgell, D. T. Michel, I. V. Igumenshchev, D. E. Hinkel, P. Michel, and J. D. Moody, "Multiple-beam laser-plasma interactions in inertial confinement fusion," *Physics of Plasmas* **21**, 055501 (2014).
- ⁴⁷R. Yan, J. Li, and C. Ren, "Intermittent laser-plasma interactions and hot electron generation in shock ignition," *Physics of Plasmas* **21**, 062705 (2014).
- ⁴⁸P. Michel, L. Divol, E. L. Dewald, J. L. Milovich, M. Hohenberger, O. S. Jones, L. B. Hopkins, R. L. Berger, W. L. Krueer, and J. D. Moody, "Multi-beam Stimulated Raman Scattering in Inertial Confinement Fusion Conditions," *Physical Review Letters* **115**, 055003 (2015).
- ⁴⁹D. T. Michel, A. V. Maximov, R. W. Short, S. X. Hu, J. F. Myatt, W. Seka, A. A. Solodov, B. Yaakobi, and D. H. Froula, "Experimental validation of the two-plasmon-decay common-wave process," *Physical Review Letters* **109**, 155007 (2012).
- ⁵⁰C. W. Lian, Y. Ji, R. Yan, S. H. Cao, C. Ren, Z. H. Wan, D. Yang, Y. K. Ding, and J. Zheng, "Two plasmon decay instability stimulated by large-incidence-angle laser in inertial confinement fusion," *Plasma Physics and Controlled Fusion* **64**, 085009 (2022).
- ⁵¹F. X. Zhou, S. H. Cao, C. W. Lian, Y. Ji, R. Yan, J. Li, D. Yang, L. Hao, C. Ren, and J. Zheng, "Large-incidence-angle multiple-beam two-plasmon decay instability in inertial confinement fusion," *Physics of Plasmas* **30**, 092702 (2023).
- ⁵²R. A. Fonseca, L. O. Silva, F. S. Tsung, V. K. Decyk, W. Lu, C. Ren, W. B. Mori, S. Deng, S. Lee, T. Katsouleas, and J. C. Adam, "Computational science — iccs 2002: International conference amsterdam, the netherlands, april 21–24, 2002 proceedings, part iii," (Springer Berlin Heidelberg, Berlin, Heidelberg, 2002) Chap. OSIRIS: A Three-Dimensional, Fully Relativistic Particle in Cell Code for Modeling Plasma Based Accelerators, pp. 342–351.
- ⁵³A. Simon, R. W. Short, E. A. Williams, and T. Dewandre, "On the inhomogeneous two-plasmon instability," *Physics of Fluids* **26**, 3107–3118 (1983).
- ⁵⁴H. Wen, F. S. Tsung, W. B. Mori, R. A. Fonseca, and L. O. Silva, "Peta-scale particle-in-cell simulations of kinetic effects in inertial fusion energy plasmas," *Plasma Physics and Controlled Fusion* **61**, 044007 (2019).
- ⁵⁵J. Zhang, J. F. Myatt, R. W. Short, A. V. Maximov, H. X. Vu, D. F. Dubois, and D. A. Russell, "Multiple beam two-plasmon decay: Linear threshold to nonlinear saturation in three dimensions," *Physical Review Letters* **113**, 105001 (2014).
- ⁵⁶J. F. Myatt, J. Zhang, J. a. Delettrez, a. V. Maximov, R. W. Short, W. Seka, D. H. Edgell, D. F. Dubois, D. a. Russell, and H. X. Vu, "The dynamics of hot-electron heating in direct-drive-implosion experiments caused by two-plasmon-decay instability," *Physics of Plasmas* **19**, 022707 (2012).
- ⁵⁷M. N. Rosenbluth, R. B. White, and C. S. Liu, "Temporal evolution of a three-wave parametric instability," *Physical Review Letters* **31**, 1190–1193 (1973).
- ⁵⁸B. B. Afeyan and E. A. Williams, "Stimulated Raman sidescattering with the effects of oblique incidence," *Physics of Fluids* **28**, 3397–3408 (1985).
- ⁵⁹W. Seka, J. F. Myatt, R. W. Short, D. H. Froula, J. Katz, V. N. Goncharov, and I. V. Igumenshchev, "Nonuniformly driven two-plasmon-decay instability in direct-drive implosions," *Physical Review Letters* **112**, 145001 (2014).